PAPER

Check for updates

Atomically precise alkynyl-protected Ag$_{19}$Cu$_2$ nanoclusters: synthesis, structure analysis, and electrocatalytic CO$_2$ reduction application†

Xin Zhu,‡[a] Pan Zhu,‡[b] Xuzi Cong,‡[c] Guanyu Ma,[a] Qing Tang, [ID] *[b] Likai Wang [ID] *[c] and Zhenghua Tang [ID] *[a,d]

We report the synthesis, structure analysis, and electrocatalytic CO$_2$ reduction application of Ag$_{19}$Cu$_2$(C≡CAr^F)$_{12}$(PPh$_3$)$_6$Cl$_6$ (abbreviated as Ag$_{19}$Cu$_2$, C≡CAr^F: 3,5-bis(trifluoromethyl)phenylacetylene) nanoclusters. Ag$_{19}$Cu$_2$ has characteristic absorbance features and is a superatomic cluster with 2 free valence electrons. Single-crystal X-ray diffraction (SC-XRD) revealed that the metal core of Ag$_{19}$Cu$_2$ is composed of an Ag$_{11}$Cu$_2$ icosahedron connected by two Ag$_4$ tetrahedra at the two terminals of the Cu–Ag–Cu axis. Notably, Ag$_{19}$Cu$_2$ exhibited excellent catalytic performance in the electrochemical CO$_2$ reduction reaction (eCO$_2$RR), manifested by a high CO faradaic efficiency of 95.26% and a large CO current density of 257.2 mA cm^{-2} at −1.3 V. In addition. Ag$_{19}$Cu$_2$ showed robust long-term stability, with no significant drop in current density and FE$_{CO}$ after 14 h of continuous operation. Density functional theory (DFT) calculations disclosed that the high selectivity of Ag$_{19}$Cu$_2$ for CO in the eCO$_2$RR process is due to the shedding of the −C≡CAr^F ligand from the Ag atom at the very center of the Ag$_4$ unit, exposing the active site. This study enriches the potpourri of alkynyl-protected bimetallic nanoclusters and also highlights the great advantages of using atomically precise metal nanoclusters to probe the atomic-level structure–performance relationship in the catalytic field.

1. Introduction

Thanks to the alloying effect, bimetallic nanoclusters usually display different physicochemical properties and functionalities from their monometallic counterparts.[1–5] Specifically, in the catalytic field, upon introducing another metal atom into the core, on the one hand, the geometric configuration of the metal nanocluster is changed and new catalytically active sites can be generated, and on the other hand, it can modulate the electronic structure of the metal nanocluster hence tuning the adsorption capacities to the reaction substrates and intermediates. For instance, the Jiang and Lee group reported that the Au$_{24}$Pt(SC$_6$H$_{13}$)$_{18}$ cluster possesses much higher hydrogen evolution reaction (HER) activity than Au$_{25}$(SC$_6$H$_{13}$)$_{18}$, as the central Pt atom can more easily form an M–H chemical bond to lower the energy barrier.[6] In another study, Deng *et al.* found that Cu doping can significantly boost the electrochemical CO$_2$ reduction reaction (eCO$_2$RR) of atomically precise Au nanoclusters. In a gas diffusion electrode-based membrane electrode assembly cell, the Au$_{15}$Cu$_4$ nanocluster exhibited a high CO faradaic efficiency (over 90%), markedly larger than that of the Au$_{18}$ cluster (~60%). Density functional theory (DFT) calculations disclosed that Cu doping induced catalytic synergistic effects, where the exposed pair of AuCu dual sites can accelerate the eCO$_2$RR process.[7] As seen above, atomically precise bimetallic nanoclusters have good catalytic activity and selectivity for the eCO$_2$RR, and more importantly, the atomically precise structure of bimetallic nanoclusters is conducive to the in-depth analysis of the reaction mechanism and the elucidation of the catalyst's structure–performance relationship at the atomic level.

[a]*New Energy Research Institute, School of Environment and Energy, South China University of Technology, Guangzhou Higher Education Mega Center, Guangzhou, 510006, China. E-mail: zhht@scut.edu.cn*

[b]*Chongqing Key Laboratory of Theoretical and Computational Chemistry, School of Chemistry and Chemical Engineering, Chongqing University, Chongqing, 401331, China. E-mail: qingtang@cqu.edu.cn*

[c]*School of Chemistry and Chemical Engineering, Shandong University of Technology, Zibo, 255049 Shandong, China. E-mail: lkwangchem@sdut.edu.cn*

[d]*Key Laboratory of Functional Inorganic Materials Chemistry, Ministry of Education, Heilongjiang University, Harbin, 150001, China*

†Electronic supplementary information (ESI) available: Experimental details, supporting figures and tables, and more calculation results. CCDC 2366717. For ESI and crystallographic data in CIF or other electronic format see DOI: https://doi.org/10.1039/d4nr02702g

‡ These authors contributed equally.

To prevent the bimetallic core from aggregation, there are various types of small molecules that can be used as capping agents or ligands for preparing bimetallic nanoclusters.[8] The ligand molecules include but are not limited to thiolate molecules,[9] N-containing molecules,[10] carbenes,[11] hydrides,[12] alkynyl molecules,[13–15] and so on. The ligand molecules can not only tune the physical and chemical properties of the metal nanoclusters,[16] but also affect the catalytic performance drastically.[17–19] The most widely employed ligand is thiolate molecules; however, alkynyl molecules as a protecting ligand have been gaining more and more research attention.[13–15] In a quite recent study, the Wang and Zhou groups reported the photophysics of $Au_{22}(^tBuPhC\equiv C)_{18}$ and $Au_{16}Cu_6(^tBuPhC\equiv C)_{18}$, where the latter exhibited >99% photoluminescence quantum yield (PLQY) in de-aerated solution at room temperature with an emission maximum at 720 nm tailing to 950 nm and 61% PLQY in an oxygen-saturated solution.[20] This is due to the fact that the Cu doping suppressed the non-radiative decay (~60-fold less) and promoted the intersystem crossing rate. Moreover, in the catalytic regime, alkynyl ligands can perturb the electronic structure of metal nanoclusters by forming σ and/or π bonds, thereby promoting the catalytic performance of some specific reactions.[20] In 2017, the Wang group fabricated two isostructural $[Au_{38}L_{20}(Ph_3P)_4]^{2+}$ (L = alkynyl or thiolate) clusters with the ligand being the only variable.[21] The alkynyl-protected Au_{38} cluster is very active in the semi-hydrogenation of alkynes with the substrate conversion ratio over 97% while the thiolate one possesses negligible activity (less than 2%). In another study, our group disclosed that, in the electrochemical CO_2 reduction reaction (eCO_2RR), alkynyl-protected Ag_{32} clusters can outcompete the phosphine and thiolate co-protected Ag_{32} clusters in terms of FE_{CO}, as the former has a much lower energy barrier for forming the key intermediate *COOH.[22] Similar phenomena have also been documented for alkynyl-protected Au_{25} nanoclusters to catalyze the HER,[23] and alkynyl-protected Au_{28} nanoclusters supported by NiFe-LDH for catalyzing the oxygen evolution reaction.[24]

So far, significant progress has been achieved on the synthesis, electronic properties, luminescent behaviours, and catalytic applications of alkynyl-protected bimetallic nanoclusters, yet the family or potpourri of alkynyl-protected bimetallic nanoclusters is still limited. For AgCu bimetallic nanoclusters, molecules with atomically precise structures and alkynyl protection only include Ag_9Cu_6,[25] $Ag_{20}Cu_{12}$,[26] $Ag_{15}Cu_6$,[27] $Ag_{22}Cu_7$,[28] $Ag_{14}Cu_2$,[29] and so on. Inspired by the above studies, herein, we report the synthesis, structural analysis, and eCO_2RR application of $Ag_{19}Cu_2(C\equiv CAr^F)_{12}(PPh_3)_6Cl_6$ nanoclusters (hereafter referred to as $Ag_{19}Cu_2$, $C\equiv CAr^F$: 3,5-bis(trifluoromethyl)phenylacetylene). $Ag_{19}Cu_2$ has characteristic absorbance features, and its overall structure was analyzed by SC-XRD. $Ag_{19}Cu_2$ exhibited excellent catalytic performance, evidenced by a high CO faradaic efficiency (FE_{CO}) of 95.26%, a high current density of 257.2 mA cm^{-2} at −1.3 V, and robust stability with no significant current decay during 14 h of continuous operation.

2.   Experimental section

See all the experimental details in the ESI.†

3.   Results and discussion

The UV-visible absorption spectrum of $Ag_{19}Cu_2$ is shown in Fig. 1a, and two characteristic absorbance peaks at 498 nm and 703 nm can be easily identified. The overall structure of $Ag_{19}Cu_2$ was then analyzed by single-crystal X-ray diffraction (Fig. 1b). Specifically, the $Ag_{19}Cu_2$ nanocluster is positively charged, with BF_4^- as the counter ion. $Ag_{19}Cu_2$ crystallizes in the $P\bar{1}(2)$ space group. $Ag_{19}Cu_2$ has 21 metal atoms in the core, which is protected by twelve $-C\equiv C-Ar^F$ ligands, six PPh_3 molecules and six chlorine ions. The calculated free valence electron number is 2, indicating that it is a superatomic cluster with a closed-shell electronic structure. In fact, after being stored at room temperature for 3 months, the absorbance features of the $Ag_{19}Cu_2$ clusters remained almost unchanged (Fig. S5†), confirming the excellent chemical stability of $Ag_{19}Cu_2$ under ambient conditions.

Subsequently, the metal core configuration of $Ag_{19}Cu_2$ was detailedly examined. As illustrated in Fig. 2a, $Ag_{11}Cu_2$ forms an icosahedron with two Cu atoms on two diagonal points, and two Ag_4 tetrahedra are connected with two faces of the two opposite sides in the $Ag_{11}Cu_2$ icosahedron to form the $Ag_{19}Cu_2$ core. Apparently, the $Ag_{19}Cu_2$ core is centrosymmetric. Interestingly, the average Ag–Ag bonding length in the $Ag_{11}Cu_2$ kernel is 2.9300 Å, slightly longer than that in the Ag_4 tetrahedra (see Fig. S2†). Next, the metal–ligand coordination mode between Ag/Cu and the alkynyl molecule was analyzed and is summarized in Fig. 2b. Basically, there are four types of coordination modes: Motif A, B, C, and D. In Motif A, the alkynyl molecule binds with three Ag atoms with σ bonding and one Ag atom with both σ and π bonding; hence Motif A adopts a μ4-η1, η1, η1, η2 coordination mode. In Motif B, the alkynyl molecule binds with four Ag atoms with σ bonding; hence the coordination mode is μ4-η1, η1, η1, η1. In Motif C, the alkynyl molecule binds with two Ag atoms with σ bonding and one Cu atom with both σ and π bonding; hence Motif C adopts a μ3-η1, η1, η2 coordination mode. Motif D has a
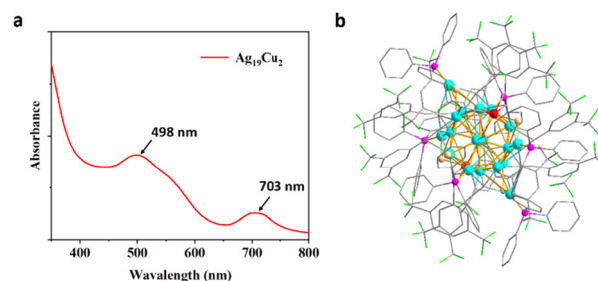

Fig. 1 (a) Absorbance spectra of the $Ag_{19}Cu_2$ nanocluster in CH_2Cl_2. (b) The overall structure of $Ag_{19}Cu_2$. Color legend: red, Cu; blue, Ag; green, Cl; purple, P; laurel green, F; white, H; gray, C.
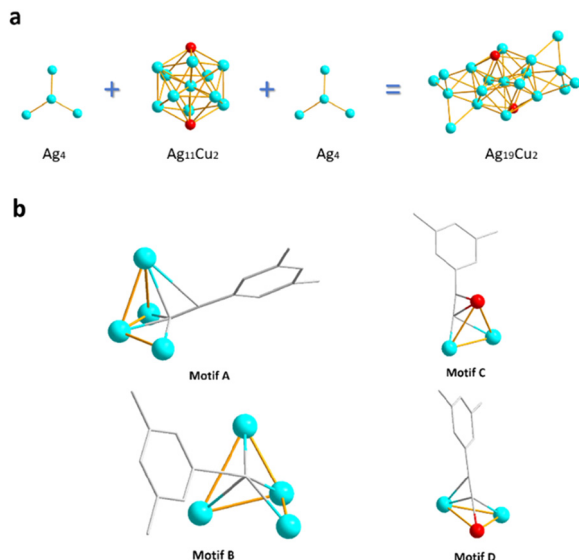
Fig. 2 (a) The structural anatomy of the $Ag_{19}Cu_2$ core. (b) Four different coordination modes between Ag/Cu and one alkynyl molecule. Color legend: red, Cu; blue, Ag; green, Cl; purple, P; laurel green, F; white, H; gray, C.

Fig. 3 (a) Polarization curve of CNTs and $Ag_{19}Cu_2$/CNTs in N_2/CO_2 saturated 1 M KOH. (b) FE_{CO} of CNTs and $Ag_{19}Cu_2$/CNTs. (c) FE_{H_2} of CNTs and $Ag_{19}Cu_2$/CNTs. (d) EE and SPCE of the eCO_2RR.

similar coordination pattern to Motif C, and the alkynyl molecule binding with both σ and π bonding is one Ag atom in Motif D but one Cu atom in Motif C; therefore, Motif D adopts a $\mu3$-$\eta1$, $\eta2$, $\eta3$ coordination mode. There are twelve alkynyl molecules capping the metal core, and the total number of Motif A, B, C, and D is 4, 4, 3, and 3, respectively. In addition, six PPh$_3$ ligands are coordinated with six Ag atoms on two sides in the cluster (Fig. S3†), and six Cl atoms are also coordinated with $Ag_{11}Cu_2$ by σ bonds in the cluster (Fig. S4†). Four Cl atoms are connected to three Ag atoms and two Cl atoms are connected to one Cu atom and two Ag atoms. All the detailed structure parameters are summarized in Table S1.†

The elemental composition and charge states of $Ag_{19}Cu_2$ were subsequently analyzed using X-ray photoelectron spectroscopy (XPS). The survey scan spectra shown in Fig. S6a† confirmed the presence of Ag, Cu, C, F, and P atoms. The high resolution XPS spectra of the Ag 3d and Cu 2p electrons in $Ag_{19}Cu_2$ can be found in Fig. S6b and S6c,† respectively. Notably, the binding energy of the Ag $3d_{5/2}$ electrons is 368.7 eV, suggesting that the valence state of Ag is between (0) and (I). Such a value is also in good agreement with the previously reported $Ag_{15}Cu_6$[27] and $Ag_{20}Cu_{12}$[26] clusters, whose Ag $3d_{5/2}$ binding energies are 368.1 eV and 368.84 eV, respectively. Meanwhile, the binding energy of the Cu $2p_{3/2}$ electrons is 933.34 eV, indicating that the valence state of Cu is (0, 1). The XPS results further validate that the superatomic cluster of $Ag_{19}Cu_2$ is successfully obtained.

The $Ag_{19}Cu_2$ nanoclusters were then loaded onto carbon nanotubes (CNTs) to investigate the eCO_2RR catalytic performance. As shown in Fig. 3a, in N_2 saturated 1 M KOH, both the CNTs and $Ag_{19}Cu_2$/CNTs exhibited no activity, while in CO_2 saturated 1 M KOH, both displayed effective activity. At the
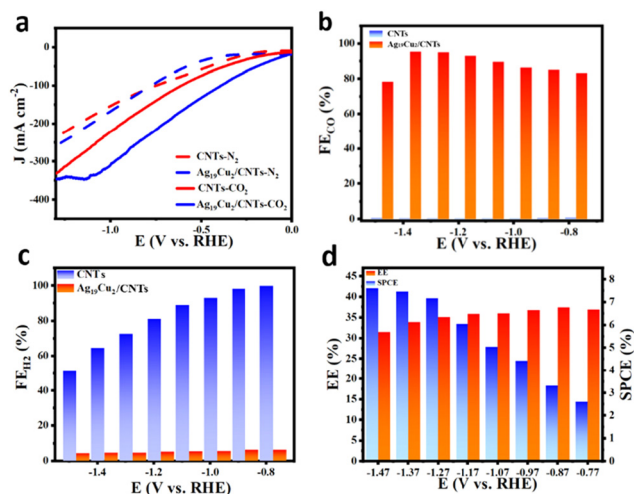
same applied potential, $Ag_{19}Cu_2$/CNTs has a much higher current density than CNTs, indicating superior catalytic activity. In the eCO_2RR, the main product is CO, along with H_2 as the side product. Faradaic efficiency (FE) is defined as the amount of product collected relative to the amount that can be produced by the total charge passing through, expressed as a fraction or percentage. In electrochemical reactions, a higher FE means that the actual power of the reaction is closer to the theoretical power and the efficiency of the reaction is higher. The FE_{CO} for $Ag_{19}Cu_2$/CNTs and CNTs is presented in Fig. 3b. The FE_{CO} for CNTs is nearly zero in the whole tested potential window, but for $Ag_{19}Cu_2$/CNTs, when the applied potential becomes more negative, the FE_{CO} first increases and then decreases, and the highest FE_{CO} is achieved at -1.37 V with a value of 95.26%. When the potential becomes quite negative, the hydrogen evolution reaction starts to dominate, which is the main reason why FE_{CO} decreases. Meanwhile, $Ag_{19}Cu_2$/CNTs displays a strong capability to suppress hydrogen evolution, as the FE_{H_2} is below 5% in the whole potential window. However, the HER process dominates the reaction for CNTs, as the FE_{H_2} increases from ~51% to nearly 100% (Fig. 3c). To further evaluate the catalytic performance of the $Ag_{19}Cu_2$/CNT catalyst, we also calculated the energy efficiency (EE), which is defined as the conversion efficiency of the chemical energy from the input electrical energy to the final product, and a higher EE means a higher yield of the reaction product and less energy wasted. From -1.47 V to -0.77 V, the EE first increased and then decreased, reaching a maximal value of 39.76% at an EE of -0.97 V (Fig. 3d). In addition, the single-pass conversion efficiency (SPCE) of the $Ag_{19}Cu_2$/CNT catalyst increased when the potential changed from -0.77 V to -1.47 V, achieving a maximal value of 7.46% at -1.47 V. Furthermore, long-term stability is another important criterion to further assess the intrinsic catalytic properties of a catalyst. As demonstrated in Fig. S7,† after continuous oper-

ation for 14 h, the current density and FE$_{CO}$ of the Ag$_{19}$Cu$_2$/CNT catalyst remained almost unchanged, suggesting excellent long-term stability.

The spin-polarized density functional theory (DFT) calculations were subsequently carried out to investigate the electrocatalytic activity and selectivity of Ag$_{19}$Cu$_2$ nanoclusters by using the Vienna *ab initio* simulation package (VASP5.4.4).[30] In order to save the computational cost, we simplified the –C≡CAr^F groups to –C≡CR (R = 3,5-C$_6$H$_3$F$_2$) and the –PPh$_3$ groups to –P(CH$_3$)$_3$, respectively. The nanoclusters were placed in a cubic box (26 Å × 26 Å × 26 Å), and their structures were optimized. The interactions of electron exchange–correlation were represented by the Perdew–Burke–Ernzerhof (PBE) functional form of the generalized gradient approximation (GGA).[31] The projector augmented-wave (PAW) method was utilized to describe the ion–electron interactions,[32] and the wave functions of all the computations were extended by a plane-wave cutoff energy of 400 eV. Only the Gamma point was used to sample the Brillouin zone, and the convergence criteria for energy and force were set as 10^{-4} eV and -0.05 eV Å^{-1}, respectively. In addition, considering the non-negligible van der Waals interactions between ligands, we used the empirical density functional dispersion (DFT-D3) method.[33]

Based on the computational hydrogen electrode (CHE) model,[34] the change in Gibbs free energy (ΔG) for each elementary step of the CO$_2$ reduction reaction and hydrogen evolution reaction can be calculated as follows:

$$\Delta G = \Delta E + \Delta ZPE - T\Delta S$$

where ΔE, ΔZPE, and ΔS represent the changes in the total energy, zero-point energy, and entropy at 298.15 K. The entropy of gas molecules is obtained from the NIST database. The entropy correction at 298.15 K and zero-point energies for CO$_2$, CO, and H$_2$ are presented in Table S2.† For the adsorbed intermediates, only the vibrational entropy calculated from the vibrational frequencies is considered. Furthermore, to address the inaccuracies in the description of CO$_2$ and CO gas-phase molecules by the PBE functional,[35,36] we added corrections of -0.34 eV and $+0.10$ eV for CO and CO$_2$, respectively.

To further understand the high eCO$_2$RR activity and selectivity of Ag$_{19}$Cu$_2$ nanoclusters observed in the experiment, DFT calculations were carried out to identify the catalytically active sites for the CO$_2$RR. To simplify the calculations, we replaced the –C≡CAr^F groups with –C≡CR (R = 3,5-C$_6$H$_3$F$_2$) groups and the –P(Ph)$_3$ groups with –P(CH$_3$)$_3$ groups, using the [Ag$_{19}$Cu$_2$(C≡CR)$_{12}$(P(CH$_3$)$_3$)$_6$Cl$_6$]$^+$ cluster as the computational model. Here, we consider all cases where the removal of a single ligand exposes under-coordinated metal active sites. We found that after the removal of the –Cl ligand, the spatial accessibility around the under-coordinated metal site (highlighted by red circles, Fig. S8†) is too small to act as a catalytic site; thus its catalytic activity is negligible. We therefore focused on the catalytic performance of Ag$_{19}$Cu$_2$ clusters after the removal of a single –C≡CR or –P(CH$_3$)$_3$ group. For the intact Ag$_{19}$Cu$_2$ cluster, –P(CH$_3$)$_3$ ligands and part of the –C≡CR ligands are attached to the Ag$_4$ unit of the Ag$_{19}$Cu$_2$

cluster, and the remaining –C≡CR ligands are connected with the Ag$_{11}$Cu$_2$ unit of the Ag$_{19}$Cu$_2$ cluster. We first consider the case of the removal of a single –P(CH$_3$)$_3$ ligand from the Ag$_4$ unit, as predicted by the free energy profile shown in Fig. 4a, where the formation of *COOH is the potential-limiting step (PDS) of the CO$_2$RR with a high reaction energy up to 1.82 eV. With the removal of a –C≡CR ligand from the Ag$_{11}$Cu$_2$ unit to form Ag$_{19}$Cu$_2$(C≡CR)$_{11}$(P(CH$_3$)$_3$)$_6$Cl$_6^+$-(1) clusters, the formation of the *COOH intermediate remains the most uphill step with a relatively high energy barrier of 1.53 eV. It is noteworthy that when a –C≡CR ligand is removed from the Ag$_4$ unit, the reaction energy for COOH* formation (PDS) on the Ag$_{19}$Cu$_2$(C≡CR)$_{11}$(P(CH$_3$)$_3$)$_6$Cl$_6^+$-(2) cluster is lower (1.09 eV). In comparison, the Ag$_{19}$Cu$_2$(C≡CR)$_{11}$(P(CH$_3$)$_3$)$_6$Cl$_6^+$-(2) cluster has a better catalytic activity for the CO$_2$RR. The optimized structures of all substrates and intermediates are depicted in Fig. S9 and S10† and Fig. 4c. We found that for the Ag$_{19}$Cu$_2$(C≡CR)$_{11}$(P(CH$_3$)$_3$)$_6$Cl$_6^+$-(2) cluster, the under-coordinated central Ag atom in the Ag$_4$ unit prefers to act as a catalytically active site for the CO$_2$RR, with both COOH* and CO* adsorbed to the central Ag atom.

Furthermore, we analyzed the competitive HER process on the surface of [Ag$_{19}$Cu$_2$(C≡CR)$_{12}$(P(CH$_3$)$_3$)$_5$Cl$_6$]$^+$, [Ag$_{19}$Cu$_2$(C≡CR)$_{11}$(P(CH$_3$)$_3$)$_6$Cl$_6$]$^+$-(1) and (2), and the free energy diagrams are shown in Fig. 4b. Our calculations show that the hydrogen-adsorption step is the potential-determining step (PDS) for the HER on the three NCs, with limiting potentials calculated to be 1.02, 0.54 and 1.24 eV respectively. All schematic presentations of the adsorption structures of intermediates are shown in Fig. S11.† Compared with the result of the electroreduction of CO$_2$ to CO, we found a contrasting product selectivity of Ag$_{19}$Cu$_2$ clusters with the removal of different ligands. Ag$_{19}$Cu$_2$ clusters after the removal of a single –P(CH$_3$)$_3$ group from the Ag$_4$ unit or a single –C≡CR group from the Ag$_{11}$Cu$_2$ unit are more favourable to undergo the HER process. However, the limiting potential of the HER (1.24
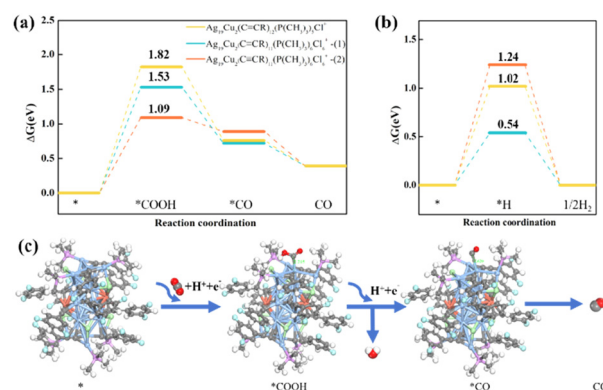

Fig. 4 Free energy diagrams (ΔG) for CO$_2$ reduction (a) and hydrogen evolution (b) on Ag$_{19}$Cu$_2$ clusters with different ligands removed at zero potential. (c) Schematic presentation of the electrocatalytic CO$_2$ reduction process on the [Ag$_{19}$Cu$_2$(C≡CR)$_{11}$(P(CH$_3$)$_3$)$_6$Cl$_6$]$^+$-(2) cluster. Colour legend: Ag, baby blue; Cu, dark orange; C, grey; Cl, light green; F, cyan; P, purple; H, white; O, red.

eV) significantly exceeds that of the CO_2RR (1.09 eV) on the $[Ag_{19}Cu_2(C{\equiv}CR)_{11}(P(CH_3)_3)_6Cl_6]^+$-(2) cluster, fully supporting the experimentally observed high CO selectivity. Overall, the DFT results suggest that the high CO selectivity of $Ag_{19}Cu_2$ clusters is probably due to the removal of the $-C{\equiv}CR$ group from the Ag_4 unit, exposing the under-coordinated Ag site as a catalytically active centre to promote electrochemical CO_2 reduction.

4.   Conclusions

In summary, we successfully synthesized an atomically precise nanocluster of $Ag_{19}Cu_2(C{\equiv}CAr^F)_{12}(PPh_3)_6Cl_6$, which possesses two valence electrons and characteristic absorbance features. The overall structure of $Ag_{19}Cu_2$ was analyzed by SC-XRD, and it has a novel $Ag_{19}Cu_2$ core composed of a $Ag_{11}Cu_2$ kernel connected by two Ag_4 units and various metal–ligand binding coordination modes. When loading into carbon nanotubes, it exhibited excellent catalytic performance, manifested by a high FE_{CO} value of 95.26%, a large CO current density of 257.2 mA cm^{-2} at -1.3 V, and robust long-term stability for a continuous 14 h test. DFT calculations revealed that the high CO selectivity is due to the shedding of the $-C{\equiv}CR$ group from the Ag_4 unit during the catalytic process, which exposes the undercoordinated Ag atom as the catalytically active site. This study enriches the family of alkynyl-protected bimetallic nanoclusters, and also provides atomic-level mechanistic insights into employing bimetallic nanoclusters as catalysts for complex electrochemical reactions.

Data availability

All data supporting the findings of this study are available within the paper and its ESI.†

Conflicts of interest

There are no conflicts to declare.

Acknowledgements

References

1 X. Kang, Y. Li, M. Zhu and R. Jin, *Chem. Soc. Rev.*, 2020, **49**, 6443–6514.

2 I. Chakraborty and T. Pradeep, *Chem. Rev.*, 2017, **117**, 8208–8271.

3 X.-M. Luo, Y.-K. Li, X.-Y. Dong and S.-Q. Zang, *Chem. Soc. Rev.*, 2023, **52**, 383–444.

4 A. Ghosh, O. F. Mohammed and O. M. Bakr, *Acc. Chem. Res.*, 2018, **51**, 3094–3103.

5 C. Sun, B. K. Teo, C. Deng, J. Lin, G.-G. Luo, C.-H. Tung and D. Sun, *Coord. Chem. Rev.*, 2021, **427**, 213576.

6 K. Kwak, W. Choi, Q. Tang, M. Kim, Y. Lee, D.-e. Jiang and D. Lee, *Nat. Commun.*, 2017, **8**, 14723.

7 G. Deng, H. Yun, M. S. Bootharaju, F. Sun, K. Lee, X. Liu, S. Yoo, Q. Tang, Y. J. Hwang and T. Hyeon, *J. Am. Chem. Soc.*, 2023, **145**, 27407–27414.

8 W. Jing, H. Shen, R. Qin, Q. Wu, K. Liu and N. Zheng, *Chem. Rev.*, 2022, **123**, 5948–6002.

9 Y. Li, M. Zhou and R. Jin, *Adv. Mater.*, 2021, **33**, 2006591.

10 S. F. Yuan, W. D. Liu, C. Y. Liu, Z. J. Guan and Q. M. Wang, *Chem. – Eur. J.*, 2022, **28**, e202104445.

11 H. Shen, G. Tian, Z. Xu, L. Wang, Q. Wu, Y. Zhang, B. K. Teo and N. Zheng, *Coord. Chem. Rev.*, 2022, **458**, 214425.

12 Y. Lv, T. Jiang, Q. Zhang, H. Yu and M. Zhu, *Polvoxometalates*, 2024, **3**, 9140050.

13 Z. Lei, X.-K. Wan, S.-F. Yuan, Z.-J. Guan and Q.-M. Wang, *Acc. Chem. Res.*, 2018, **51**, 2465–2474.

14 X. Ma, Y. Tang, G. Ma, L. Qin and Z. Tang, *Nanoscale*, 2021, **13**, 602–614.

15 L. Chen, L. Wang, Q. Shen, Y. Liu and Z. Tang, *Mater. Chem. Front.*, 2023, **7**, 1482–1495.

16 Y. Wang, Z. Liu, A. Mazumder, C. G. Gianopoulos, K. Kirschbaum, L. A. Peteanu and R. Jin, *J. Am. Chem. Soc.*, 2023, **145**, 26328–26338.

17 Q. J. Wu, D. H. Si, P. P. Sun, Y. L. Dong, S. Zheng, Q. Chen, S. H. Ye, D. Sun, R. Cao and Y. B. Huang, *Angew. Chem., Int. Ed.*, 2023, **62**, e202306822.

18 H. Shan, J. Shi, T. Chen, Y. Cao, Q. Yao, H. An, Z. Yang, Z. Wu, Z. Jiang and J. Xie, *ACS Nano*, 2023, **17**, 2368–2377.

19 Z. Liu, H. Tan, B. Li, Z. Hu, D.-e. Jiang, Q. Yao, L. Wang and J. Xie, *Nat. Commun.*, 2023, **14**, 3374.

20 W.-Q. Shi, L. Zeng, R.-L. He, X.-S. Han, Z.-J. Guan, M. Zhou and Q.-M. Wang, *Science*, 2024, **383**, 326–330.

21 X.-K. Wan, J.-Q. Wang, Z.-A. Nan and Q.-M. Wang, *Sci. Adv.*, 2017, **3**, e1701823.

22 L. Chen, F. Sun, Q. Shen, L. Qin, Y. Liu, L. Qiao, Q. Tang, L. Wang and Z. Tang, *Nano Res.*, 2022, **15**, 8908–8913.

23 X. Li, S. Takano and T. Tsukuda, *J. Phys. Chem. C*, 2021, **125**, 23226–23230.

24 Q.-L. Shen, L.-Y. Shen, L.-Y. Chen, L.-B. Qin, Y.-G. Liu, N. M. Bedford, F. Ciucci and Z.-H. Tang, *Rare Met.*, 2023, **42**, 4029–4038.

25 X. Ma, F. Sun, L. Qin, Y. Liu, X. Kang, L. Wang, D.-e. Jiang, Q. Tang and Z. Tang, *Chem. Sci.*, 2022, **13**, 10149–10158.

26 G. Ma, F. Sun, L. Qiao, Q. Shen, L. Wang, Q. Tang and Z. Tang, *Nano Res.*, 2023, **16**, 10867–10872.

27 G. Deng, J. Kim, M. S. Bootharaju, F. Sun, K. Lee, Q. Tang, Y. J. Hwang and T. Hyeon, *J. Am. Chem. Soc.*, 2022, **145**, 3401–3407.

28 G. Deng, K. Lee, H. Deng, S. Malola, M. S. Bootharaju, H. Häkkinen, N. Zheng and T. Hyeon, *Angew. Chem., Int. Ed.*, 2023, **62**, e202217483.

29 Q. Shen, X. Cong, L. Chen, L. Wang, Y. Liu, L. Wang and Z. Tang, *Dalton Trans.*, 2023, **52**, 16812–16818.

30 G. Kresse and J. Furthmüller, *Phys. Rev. B: Condens. Matter Mater. Phys.*, 1996, **54**, 11169–11186.

31 J. P. Perdew, K. Burke and M. Ernzerhof, *Phys. Rev. Lett.*, 1997, **78**, 1396–1396.

32 I. L. Garzón and A. Posada-Amarillas, *Phys. Rev. B: Condens. Matter Mater. Phys.*, 1996, **54**, 11796–11802.

33 J. K. Norskov, J. Rossmeisl, A. Logadottir, L. Lindqvist, J. R. Kitchin, T. Bligaard and H. Jónsson, *J. Phys. Chem. B*, 2004, **108**, 17886–17892.

34 A. A. Peterson, F. Abild-Pedersen, F. Studt, J. Rossmeisl and J. K. Norskov, *Energy Environ. Sci.*, 2010, **3**, 1311–1315.

35 P. E. Blöchl, *Phys. Rev. B: Condens. Matter Mater. Phys.*, 1994, **50**, 17953–17979.

36 Q. Tang, Y. Lee, D.-Y. Li, W. Choi, C. W. Liu, D. Lee and D.-e. Jiang, *J. Am. Chem. Soc.*, 2017, **139**, 9728–9736.